Chapter 13
X-Ray Spectroscopy with XFELs

Roberto Alonso-Mori and Junko Yano

13.1 Introduction

Many important redox-active metalloenzymes employ 3d transition metals (TM) in their active sites to catalyze multi-electron reactions at ambient temperature and pressure in aqueous solution. While these catalysts cannot simply be transferred into industrial processes, they provide important information on how to spatially and temporally control electron and proton flow and product/substrate transport during chemical transformations. X-ray spectroscopy at synchrotron radiation (SR) facilities has contributed significantly to the structural and functional studies of those metalloenzymes in the past decades. Owing to its element sensitivity and less-restrictive sample environment, it has been an essential method to study geometric and electronic structures of metal catalytic centers in the complicated biological environment. However, to minimize or eliminate radiation-induced changes during data collection has been challenging, and the measurements are typically carried out at cryogenic temperature (liquid nitrogen or liquid helium) to prevent the destruction of samples from the diffusion of radicals [1–3]. At the same time, there is increasing desire to understand biological phenomena as the enzymes function, i.e., under physiological conditions.

X-ray free electron lasers (XFELs) have shown the potential for being a transformative tool for studying biological systems under physiological conditions. The X-ray pulses generated by an XFEL are extremely intense with short pulse

R. Alonso-Mori (✉)
Linac Coherent Light Source, SLAC National Accelerator Laboratory, Menlo Park, CA, USA
e-mail: robertoa@slac.stanford.edu

J. Yano
Molecular Biophysics and Integrated Bioimaging Division, Lawrence Berkeley National Laboratory, Berkeley, CA, USA
e-mail: jyano@lbl.gov

S. Boutet et al. (eds.), *X-ray Free Electron Lasers*,
https://doi.org/10.1007/978-3-030-00551-1_13

widths, containing as many photons ($>10^{12}$) in one pulse (typical pulse length <100 fs) as most SR beamlines generate in 1 s. Moreover, the focused X-ray beam is generally very small in size, typically 1–5 μm and in some instruments even down in the nm range, enabling the study of very small samples and providing very high fluence. These unique properties of the XFEL pulses enable, within a set of conditions, shot-by-shot radiation damage-free data collection (see Sect. 13.2 "Radiation Damage" below); the ultrafast pulse (fs) is faster than the damage caused by the diffusion of hydroxo radicals or solvated electrons (ps). This results in collection of spectroscopic data, diffraction patterns, or other measurements at room temperature without relying on cryo-techniques that are the norm for X-ray studies at SR sources. This capability leads to the possibility of following structural and electronic changes in biological systems in real time, as the reaction proceeds. XFEL pulses can be used to access fs to early ps time regime phenomena, which is not possible at the current SR sources, except for laser-electron slicing facilities that provide orders of magnitude fewer photons. Owing to advancements in the timing systems (time tools based on crystals and gratings at the LCLS and SACLA, respectively [4]), the effect of the XFEL timing jitter on temporal resolution can be reduced down to tens of fs. On the other hand, the velocity mismatch between the X-ray "probe" and optical "pump" beams is still the limiting factor in many cases, and the resolution of most time-resolved studies is currently ~50–100 fs.

To take full advantage of the benefits of the XFELs for the mechanistic studies of biological samples, there are additional challenges that include preparing and delivering the samples efficiently, triggering chemical reactions in situ, and the data analysis in shot-by-shot mode. The sample needs to be replenished at the repetition rate of the X-ray laser as it is destroyed after each pulse, making solutions in liquid jets being the best candidates for spectroscopy experiments. New analysis routines to handle the shot-to-shot characteristics of the signal and the instabilities of the probed sample and the XFEL beam have to be established. In addition, one needs to consider other unique characters of the XFEL X-rays such as the SASE (Spontaneous Amplified Stimulated Emission beam) [5] bandwidth, shot-by-shot fluctuations of the beam (in intensity, spectral energy, timing, and space), and possible nonlinear effects due to the extreme fluence deposited on the sample (see Sect. 13.2 below).

In this chapter, we discuss various X-ray spectroscopy methods that are useful for studying biological systems. While a large part of the current biological XFEL research is centered on crystallography, the spectroscopic techniques are required to obtain electronic structural information at specific metal sites. The element sensitivity of X-ray spectroscopy uniquely provides geometric and electronic information of the metal site in both crystalline and solution samples. Such information will help bridging between protein dynamics and chemical changes in metalloenzymes, *e.g.*, how the protein environment modulates the site for the catalytic reaction to occur through sequential events during the reaction. Furthermore, simultaneous detection of X-ray crystallography and spectroscopy is possible under some experimental conditions in XFELs, and the method contributes to a seamless understanding of structural dynamics of proteins and chemical dynamics at the metal centers.

We discuss here X-ray absorption spectroscopy (XAS), nonresonant X-ray emission spectroscopy (XES), and resonant inelastic X-ray scattering (RIXS), and how to adapt them to exploit the XFELs' particularities described above. Thereafter, we will summarize the application of these spectroscopic techniques to the study of biologically relevant systems reported in the past few years since XFEL sources became available, in particular at LCLS (Linac Coherent Light Source) [6] and SACLA (SPring-8 Angstrom Compact Free Electron Laser) [7].

13.2 Radiation Damage

The term "radiation damage" can be used to describe different phenomena, each having a unique impact and requiring a different response when performing spectroscopy experiments. Radiation damage can be due to: (1) the diffusion of radicals or solvated electrons created by the interaction of X-rays and water, (2) Coulomb explosion when the fluence is high enough to break the bonds holding the molecules together, and (3) nonlinear effects when the fluence is high enough to enhance these low cross section electronic phenomena.

Traditionally, the main cause of "radiation damage" at SR-based experiments in biological systems is the diffusion of solvated electrons and radicals created by the interaction of X-rays and water. The interaction of these species with the sample causes the reduction of highly oxidized metals, the breakage of disulfide bonds and the decarboxylation of carboxylate residues among others. Therefore, at SR facilities data collection for crystallography and spectroscopy experiments is usually carried out at cryogenic temperatures to minimize or eliminate radiation-induced changes. Lowering the temperature reduces the diffusion of radicals, thus decreasing damage to the proteins and lipid environment. The diffusion of radicals/solvated electrons occurs in the sub-ps to ps range, so another way to avoid their effects is to outrun this process by collecting data in a faster timescale. The ultrashort fs X-rays at XFELs thus allow collecting data from the intact form of a system, free from this secondary radiation damage due to radical diffusion, even at room temperature, permitting the study of biological systems in their functional form in native-like conditions.

At XFELs though, one needs to consider the consequences of the intense X-ray pulses depositing its energy into a small sample volume. The photoionization of the irradiated sample, which also causes the formation of the free radicals, can cause a residual positive charge to accumulate at the sample. When the X-ray pulse fluence is high enough such that the electric charge due to the photoionization can break the molecule bonds, a Coulomb explosion occurs [8–10]. In this chapter, we will refer to this as "electronic damage," to differentiate it from the diffusion-based radiation damage described earlier. The first step of the phenomenon involves stripping off multiple electrons. Its repercussions for structural studies are prominent and are discussed in more detail in Chap. 6 in this book. The intense X-ray pulses can increase the probability of nonlinear effects (which have generally a very low cross

section), where the relation between the incoming X-ray fluence and the outgoing signal intensity is not linear anymore. Nonlinear effects include many phenomena (e.g., two-photon absorption, double core-hole excitation, sequential ionization, X-ray-induced transparency, or stimulated emission) and their study may lead to novel applications. However, for standard spectroscopy experiments, one consequence is that the spectra of interest may be distorted as compared with the spectra observed in the linear-response regime. This effect has been observed at XFELs, with tightly focused hard X-ray beams, and even more pronounced in the soft X-ray regime in which the absorption cross section is larger. To avoid this, one needs to reduce the focus or attenuate the beam. This is a dilemma, in particular, for some of the photon-hungry experiments like RIXS on dilute systems. In general, hard X-ray spectroscopy measurements carried out with "standard" XFEL fluences (few μm focus and $\sim 10^{11}$ ph/pulse) still preserve the spectral shape and yield valid chemical information. This has been demonstrated by early XES studies at LCLS, conducted with Mn inorganic compounds in solution, and the comparison with spectra collected at SR at cryogenic temperature [11]. For experiments or techniques requiring tighter focus, or more prone to this type of damage, having a higher repetition rate rather than increasing the fluence is a preferable approach.

13.3 Methods

13.3.1 Sample Delivery

A single XFEL pulse can damage or destroy the probed volume, especially when using a focused beam, making it necessary to replenish the sample between shots. Therefore, developing methods for consistently delivering a homogeneous sample to the X-ray beam in a synchronous way is critical for XFEL applications. A few different approaches have been used based on the needs of the application, e.g., sample type, volume available, sample environment, or reaction-triggering method. Most spectroscopic applications at XFELs rely on using liquid jets, where a solution (or suspended small particle/crystal) is continuously transported from a reservoir through a capillary and ejects at the interaction region. At low repetition rates, only a small fraction of the sample volume is probed by the pulsed XFEL beam. In some cases, this allows recirculating the sample through a closed-loop system if the sample is limited. For spectroscopy experiments, the stability of the jet is fundamental, in particular for resonant techniques where normalization of the signal for each shot is critical. Moreover, these photon-hungry techniques require thick liquid jets, ideally on the order of the absorption length. When sample availability is not an issue, round Rayleigh or sheet jets are preferred, providing excellent stability for diameters above 10 μm, with sample consumption in the ml/min range. Round jets with hundreds of nm diameter and sheet jets with thickness above 100 μm have also been used at LCLS. More details can be found here [12].

When the sample is limited, other injection systems can be used, including droplet systems. The Rayleigh flow can be broken up by compression (e.g., by a piezoelectric device) to create a stable train of drops [13], thus eliminating the sample volume loss in between X-ray pulses. Another drop-based system is the acoustic droplet injector (ADE) [14, 15] where liquid drops are ejected from a well reservoir by means of focused sound waves synchronized with the XFEL repetition rate. For time-resolved experiments that require longer time delays of ms to few s time range, the ADE can be combined with a drop on tape (DOT) system, where a conveyor belt system transports the droplets to the X-ray beam through the reaction region (e.g., light or gas activated) [16]. The flow rate of these systems is in the 10 μl/min range.

Finally, for applications where the sample is in the solid state, fixed targets continuously scanned through the XFEL beam have been used at LCLS [17–19], allowing up to 120 Hz data collection. For more details on sample delivery systems tailored for XFEL applications, see Chap. 5 in this book.

13.3.2 X-Ray Absorption Spectroscopy

X-ray absorption spectroscopy (XAS) as we know it today has been utilized since the mid-1970s, concomitantly with the advent of the first SR sources. During all these years, it has greatly contributed to the advancement of many fields, from material science to biology, due to its element specificity and sensitivity to changes in the electronic structure and local coordination of the selected element. XAS studies photoinduced transitions of an electron from a core state to low-energy, empty molecular orbitals above the Fermi energy, probing the density of unoccupied electronic states [20] (see Fig. 13.1). The first tens of eV of an XAS spectrum, the X-ray absorption near edge structure (XANES) region, arises from transitions close to the Fermi level that may include bound states (resonant excitations). XANES provides chemical information, and the position of the absorption edge indicates the valence states, while its shape yields information about the coordination environment of the absorber. As shown in Fig. 13.2a, the region including the following few hundreds of eV is called extended X-ray absorption fine structure (EXAFS), and it is dominated by scattering processes. Here, the highly energetic photons liberate photoelectrons that propagate from the absorber atom and are backscattered by neighboring atoms producing interference and the characteristic EXAFS oscillations. From the EXAFS signal, it is possible to determine the atomic number, distance, and coordination number of the atoms surrounding the absorber.

Transmission detection is the only direct approach to measure the absorption coefficient, where the XAS spectrum is obtained by measuring the beam intensity going through the sample while scanning the incident energy across the edge. However, this approach is not straightforward for soft X-rays, where the attenuation length of few micrometers implies that the sample has to be extremely thin. The absorption coefficient can also be approximated indirectly with total fluorescence

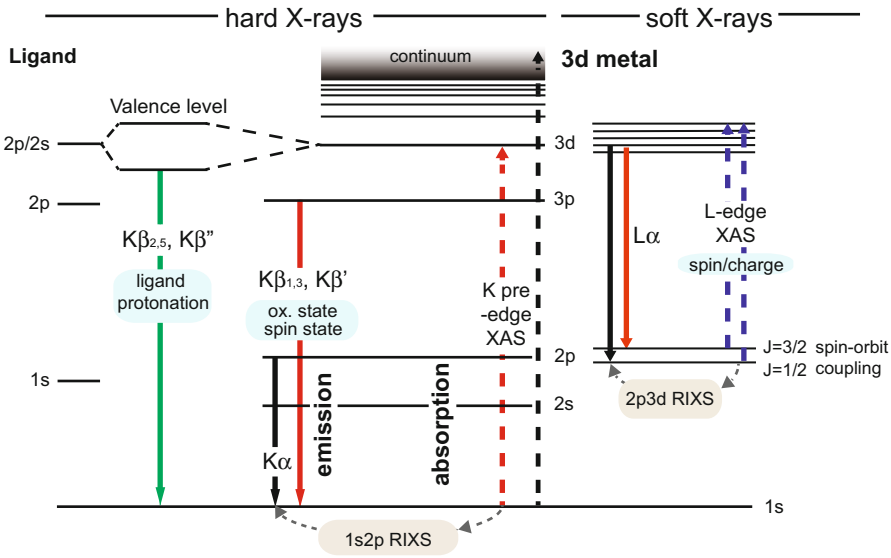

Fig. 13.1 Energy diagram levels for 3d transition metals showing the characteristic transitions relevant for hard X-ray and soft X-ray spectroscopy techniques

yield (TFY) detection, where the spectrum is obtained by recording the radiation produced in the decay process after the occurrence of the absorption event. TFY is generally applied in the soft X-ray range as well as in the hard X-ray range for diluted samples that do not absorb enough photons to obtain a XAS spectrum in transmission mode. While transmission and TFY are routinely applied at SR sources, various factors have to be taken into account to transfer these spectroscopic approaches to XFEL experiments.

XAS requires a highly monochromatized incident beam (typically $< \Delta E = 10^{-4}$) and the incident X-ray energy needs to be scanned in a wide energy range (XANES: 50 eV, EXAFS: 500 eV). As the SASE radiation from XFELs has a spectral width on the order of $\Delta E/E = 10^{-3}$, the use of an incident beam monochromator, to scan specific energies across the absorption edge, is necessary. The use of SASE presents some drawbacks. Due to the broad SASE spectral bandwidth and also its structure (composed of multiple peaks fluctuating in position and intensity from pulse to pulse), the average transmission through the monochromator is only few percent with 100% intensity variations pulse to pulse. As an alternative to the use of SASE in combination with a beamline monochromator, the use of a more monochromatic self-seeded beam (demonstrated for soft and hard X-rays at LCLS with a bandwidth down to $\Delta E = 10^{-4}$) [21] has been explored. This could in principle eliminate the need of a beamline monochromator and provide higher monochromatic flux. However, in some cases the use of a monochromator is still required to filter out the significant SASE background present in the spectrum [22]. Improvements in accelerator technology could improve the performance of self-

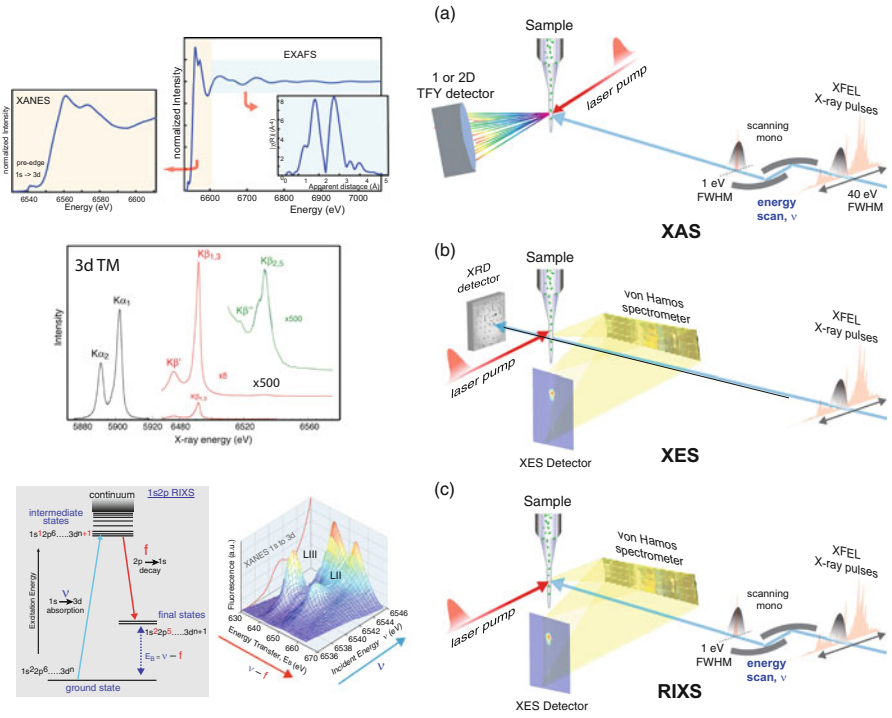

Fig. 13.2 Schematic of hard X-ray XAS, XES, and RIXS spectroscopic experimental setups for a typical XFEL pump-probe liquid jet experiment, and the spectroscopic signals are collected at variable time delays after laser pump. **(a)** In an XAS experiment, the TFY signal is recorded with a diode or a 2D detector while scanning the incident energy by means of a monochromator. XANES (scanning the first ∼50 eV) to obtain chemical information or EXAFS (scanning the first ∼500 eV) spectra to obtain structural information can be collected with this setup. **(b)** The XES signal is collected by means of a dispersive spectrometer with no scanning elements for either the incident or the emitted beams. This technique is compatible with the simultaneous collection of XRD/XDS data in forward scattering geometry. **(c)** RIXS setup requiring both the scanning of the incident energy and the high-resolution spectrometer to record the emitted spectra. XES-type spectra are recorded while scanning the incident beam through the absorption edge to reconstruct a RIXS map. **(Left)** Energy level diagram showing the electronic levels and decay channels involved in a 1s2p measurement and the corresponding RIXS plane

seeding in the future. Additionally, the thermal load in the upstream optics can cause spatial and spectral drifts and induce unreliable measurements. All these experimental aspects inherent to XFELs make it clear that accurate beam diagnostics and normalization protocols, both for the incident X-ray properties (intensity and spectrum) and for sample variations (probed volume and concentration), are critical to obtain a reliable spectrum and reduce systematic errors.

Despite the above challenges, several pump-probe XAS experiments have been realized at XFELs in the past few years. In the hard X-ray regime, Lemke et al. [23] demonstrated that the inherent instabilities of the SASE beam can be overcome

and high-quality time-resolved XANES data can be measured on a spin-crossover system. The setup is depicted in Fig. 13.2a, in which they used a photodiode placed at 90 degrees from the sample to capture the TFY signal from the aqueous solution of $[Fe(bpy)_3]^{2+}$. More recent measurements at LCLS have shown that the use of a fast 2D detector with high-energy resolution could improve data quality by collecting the spectra in partial fluorescence yield (PFY) mode, i.e., approximating the absorption coefficient by measuring a single emission line, usually the stronger $K\alpha$, discriminated against other signals. A liquid jet in He environment was used to replace the solution sample after each shot and avoid electronic damage by the intense XFEL pulses. A similar setup was used in subsequent XANES experiments to study the early dynamics of photoexcited reactions of molecular complexes and proteins in solution at the LCLS [24–28]. Though most of the XFEL XANES studies were based on TFY methods, a potential alternative relies on the use of transmissive spectrometers. By subtracting the spectral signal between two spectrometers located upstream and downstream of the sample, the absorption spectrum can be obtained on a single shot basis, allowing self-normalization of the fluctuating source spectral content and more efficient data collection compared to scanning the upstream monochromator. This method has been demonstrated for concentrated samples [29] at LCLS. A similar method developed at SACLA uses a transmissive grating to split the XFEL beam and collect dispersive XAS data [30]. This approach was used for time-resolved XAS studies of 0.1 and 1 M ammonium ferroxalate solutions [31, 32]. Yet another dispersive approach was used at LCLS by Gaudin et al. [33] to measure the Mo L3 edge from a solid sample. No EXAFS study has been yet realized at an XFEL, mainly due to the requirement of the long-range energy scan (about 500 eV), but also to the high sensitivity required to capture changes in the EXAFS region, on the order of few percent changes. This makes it very challenging to measure EXAFS spectra on very diluted biological systems. The foreseen average flux increase, accomplished via higher repetition rates, provided by LCLS-II and the European XFEL will make EXAFS studies possible.

At SR sources, metal K-edge spectroscopy has been widely used for biological spectroscopy of 3d TM. On the other hand, metal L-edge spectroscopy, which falls into the soft X-ray energy range (approximately <2000 eV), has been rarely used for biological systems. This is largely because of severe radiation damage that occurs even at cryogenic temperatures, as the absorption cross section is about 100 times larger than that of K-edges. The larger absorption cross section also implies that the X-ray penetration depth is much shallower (for example, the attenuation length is 0.8 μm at 650 eV) than that of hard X-rays (500 micrometer at 6500 eV), making the soft X-ray spectroscopy methods a semi-surface sensitive tool. Furthermore, the requirement of ultrahigh vacuum, which dehydrates samples, makes the experiments with biological samples more difficult. Despite such challenges, there are several advantages in using metal L-edge spectroscopy. It has significantly better resolution, as the natural line widths at the L2 and L3 edges are approximately one-fourth of those at the K-edge due to the longer core-hole lifetime. This makes L-edge spectra more informative about the electronic structure [20, 34]. The 2p to 3d transitions are allowed under dipole selection rules (the atomic orbital angular momentum

$\Delta 1 = +/-1$). On the other hand, the pre-edge peak (1s–3d transitions) at K-edge spectroscopy that is widely used for extracting the electronic structure is weak as it is quadrupole-allowed ($\Delta l = 0, +/-2$), and often overwhelmed by the dipole-allowed main edge intensity. Therefore, L-edge spectroscopy has a greater sensitivity to the occupancy and interactions of the metal 3d-derived orbitals and can provide a better indication of the bonding, oxidation/spin states, and symmetry of the complex involved.

Biological soft X-ray spectroscopy at XFELs is just at the stage of its birth, but the collection of X-ray damage-free data at room temperature would be of particular advantage for biological systems if a suitable detection scheme is developed. Such a detection scheme needs to probe the spectroscopic signal in the dilute sample arising from the metal L-edges at 400–1000 eV, while separating it from the strong $K\alpha$ background signal of the light elements in the sample (C, N, O with absorption K-edges at 280–540 eV). This can be realized with an energy discriminating scheme as the element-specific PFY detection. Grating spectrometers have been commonly used for PFY detection techniques at SR sources. However, these instruments have not been successfully used so far for dilute samples due to their small subtended solid angle. Another approach is to use a superconducting tunnel junction (STJ) detector [35], which presently provides ~20 eV resolution; efforts are undergoing to improve the resolution and solid angle of these detectors. A more robust way of detecting fluorescence signals has been recently developed, using a high-reflection zone-plate spectrometer to spatially separate the metal $L\alpha$ signal from the background [36]. The solid angle of the zone-plate spectrometer is several times higher than that of gratings or STJs. This method [36, 37] (see Fig. 13.3a) has been demonstrated to overcome the experimental difficulties of metal L-edge spectroscopy, and opened the way to the use of soft X-ray spectroscopy as a unique and powerful tool to study metalloenzymes in physiological conditions and catalytic reactions in dilute solution environments. More details can be found in Sect. 13.4.

In addition to the efficient signal collection described above, soft XAS on dilute samples at XFELs often faces the challenge of a limited number of incoming photons. In standard soft XAS experiments, the incoming X-rays are monochromatized with gratings and the absorption energy range is scanned continuously or step-wise, significantly attenuating the beam in the process (~20% reflectivity). As a consequence of the use of the monochromator and its related losses, the monochromatic peak flux on the sample is reduced down to a few percent of the original peak flux (depending on the selected resolving power by the bandwidth narrowing exit slit of the monochromator). This reduced monochromatic photon flux is a limitation for XAS data collection for dilute samples like metalloenzymes (at the mM level) and specially for more photon-hungry techniques like RIXS that require a high average flux. One way to address this limitation at XFELs is using the self-seeding mode of operation described above, where the monochromatization is performed before the laser amplification. As a consequence, one can obtain a higher spectral brightness as compared to SASE where the monochromatization is done after lasing. One can therefore expect an improvement for soft XAS by

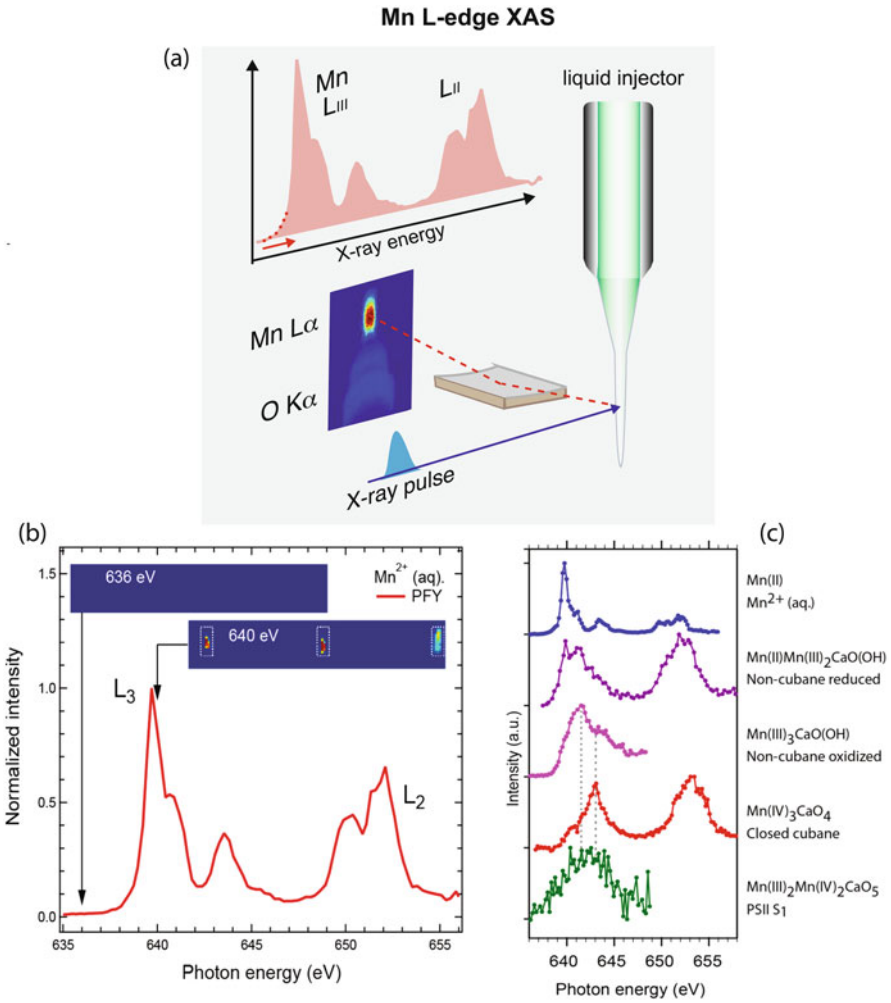

Fig. 13.3 **(a)** Soft XAS setup based on zone plates allowing the geometric discrimination of the metal signal from the Oxygen background from a solution sample. Reproduced with permission from [36]. **(b)** Mn L-edge partial fluorescence yield (PFY) XAS spectrum from $MnCl_2$ (500 mM) aqueous solution (above two CCD images in the pre-edge and L3-edge regions). Reproduced with permission from [36]. **(c)** Mn L-edge PFY XAS spectra of solutions of inorganic models (500 mM Mn^{2+}_{aq} solution, three inorganic Mn_3CaOx model complexes with Mn concentrations of 6–15 mM) and from Mn_4CaO_5 cluster in PSII (S1 dark resting state, Mn concentration of 0.8 mM). Reproduced with permission from [37]

a narrower bandwidth which leads to a higher peak and average flux in the self-seeding mode. The use of the self-seeding scheme for soft XAS data collection has been shown by Kroll et al. [22]. The study shows that the spectrum of the seeded pulse is narrow and clean enough to allow direct use for XAS data collection without

the additional beamline monochromator, and that it could lead to a factor of 3–5 increase in average flux. In the soft X-ray energy regime, one also needs to be aware of a higher possibility of sequential absorption of multiple X-ray photons by the same atom due to the large absorption cross section, which reduces the peak intensity [38]. For this reason, a higher repetition rate of the XFEL pulses is often more desirable than higher fluence per pulse for efficient data collection.

13.3.3 Nonresonant XES

Subsequent to the X-ray absorption process, the atom, in an excited state, spontaneously decays by emitting XES signal (also called fluorescence). Nonresonant XES, where the excitation energy is well above the absorption edge, gives access to different information by probing different decay channels. K emission lines of 3d TM (Kα, K$\beta_{1,3}$, $K\beta'$, $K\beta_{2,5}$, and $K\beta''$) in the hard X-ray regime, shown in Fig. 13.1, provide information on the oxidation state, effective spin, and the metal bonding orbitals [39]. In the soft X-ray range, L emission lines are a direct probe of the 3d electronic structure, providing chemical sensitivity to oxidation states, symmetry, and covalency of the system under study (see Fig. 13.1). XAS and XES are complementary techniques, providing information about unoccupied and occupied states, respectively. XES is not as ubiquitous as XAS at SR sources. This is in part because it is more complex experimentally, requiring additional instrumentation. High-resolution emission spectrometers, generally based on perfect Si/Ge crystal analyzers with reflections matching emission lines in a close-to-backscattering geometry, are required. Nonresonant XES techniques are more favorable at XFELs since the broad bandwidth of the pulse and its spectral and intensity fluctuations have no effect on the XES spectrum, and therefore no monochromator is necessary, avoiding the associated problems described in the previous section. Moreover, the use of a dispersive detection method enables the collection of spectra in single shots, which is beneficial when dealing with the pulse-to-pulse fluctuations of the SASE beam, and eliminates normalization issues. In the hard X-ray regime, dispersive setups can be realized based on the von Hamos geometry [40]. In this approach, one or more cylindrically bent dispersive crystal analyzers diffract the spectral energy range (by means of Bragg's law) onto the detector. The axis along the sample and detector positions and the axis along the crystal analyzer(s) surface are parallel to each other and separated by a distance equal to the crystal(s) bending radius. A multi-crystal von Hamos spectrometer deployed at LCLS is described here [41] and adaptations of this design are being deployed in other XFEL sources. Dispersive instrumentation requires a 2D detector to capture the extended signal reflected by the crystal analyzers, which is then integrated over the dispersive direction to obtain the XES spectrum. Various studies have been performed at XFELs using this type of instrumentation (see Fig. 13.2b). Alonso-Mori et al. [11] demonstrated that it is feasible to use hard X-ray spectroscopy at LCLS to provide reliable information on the intact electronic structure of redox-active compounds without being affected

by electronic damage caused by the intense XFEL pulses. Subsequent studies at LCLS and SACLA include measurements of photoinduced charge transfer and spin dynamics in coordination complexes [42–47] and of the redox state of photoactive proteins [16, 48–50]. In some of these experiments, the von Hamos dispersive approach was complemented by simultaneous collection of a single spectral energy from the same or a different emission line with a point-to-point Rowland setup (using spherically bent crystal analyzers) [51], which is convenient to follow the kinetics of the reaction. An important advantage of dispersive XES is that it can be easily combined with forward scattering data collection since both setups are located in orthogonal geometries. Both signals can therefore be collected simultaneously from the same pulse, and many of the previously cited examples have exploited these features to monitor the electronic structure of proteins, such as Photosystem II through its reaction cycle, while collecting X-ray diffraction data [48, 49] and to follow spin state changes while measuring X-ray diffuse scattering [44, 45, 47]. To date, no studies using the weaker $K\beta_{2,5}$ have been performed at XFELs. $K\beta_{2,5}$ is ~50 to 80 weaker than $K\beta_{1,3}$ and new methods/improved setups need to be developed to collect this valence to core transition on diluted samples. LCLS-II, with its increased average incident flux, will make these studies on biological systems possible. For a more detailed discussion on hard X-ray XES instrumentation and experiments at the LCLS, see here [52].

The tender X-ray regime (typically between 2 and 5 keV) has historically not been widely accessible at X-ray sources. However, this is an interesting range since it enables probing the electronic structure of elements that are ubiquitous in biological systems, including 4d TM L-edges (e.g., Ru, Mo, and Ag), and the K-edges of lower Z elements (e.g., P, S, and Cl). Not many SR facilities have spectrometers covering this energy range and therefore only few spectroscopic studies have been realized up to now [53, 54], in particular for resonant techniques [55]. This is because the transmission of hard X-ray beamlines decays very rapidly when decreasing the energy to this range, and because of the difficulties of developing emission spectrometers with convenient crystal reflections for these energies. SwissFEL will be able to access this energy range, and efforts are also undergoing to make instruments at LCLS-II compatible with the tender X-ray regime. Von Hamos-based spectrometers with newly developed crystal analyzers are being explored for LCLS and will be able to probe the tender energy range in a close-to-backscattering geometry, improving the efficiency of previous designs by about tenfold. These developments will enable fs and ps time-resolved experiments to study the electronic structure of elements that are not accessible elsewhere. This setup can be applicable not only to XES but also to other spectroscopic techniques like XAS and RIXS.

For the soft X-ray regime, XES has not been applied to biologically relevant systems at XFELs. This is due to the difficulties of collecting emission signals efficiently, in addition to the current limitation of the incoming X-ray photons at XFELs (namely, the average flux is not high enough to collect data within a reasonable time for dilute samples). The details can be referred to in Sect. 13.3.2, in which we described the PFY-detected XAS methods. In the nonbiological molecular

systems, however, the method has been applied to study ultrafast phenomena of a transiently populated state in CO desorption from Ru(0001) with pump-probe technique [56, 57]. The detection of photoelectrons has also been applied to study various chemical processes in the soft X-ray regime [57–59].

In general, XES data collection is not very efficient as even advanced multi-analyzer spectrometers can only cover a fraction of the signal emitted isotropically by the sample through spontaneous processes. However, the high fluence provided by XFELs can be used to stimulate the X-ray emission process. This is achieved when the incoming X-ray pulses produce sufficient ions to invert the population to an excited state along the path of the X-ray beam. The subsequent decay along the beam direction results in stimulated emission processes leading to a strong amplification gain. The advantage of this method is twofold: (1) the strong directionality of the stimulated process makes it very easy to collect the emission signal, for example, by a flat crystal downstream of the sample in the hard X-ray regime, removing the need of complicated X-ray emission spectrometers, and (2) the amplification increases the signal strength by many orders of magnitude. Taken together, these effects can dramatically decrease data collection time and increase sensitivity. This approach has been already demonstrated both in the hard [60] and soft [61] X-ray regimes.

13.3.4 RIXS

Beyond more conventional XAS and XES approaches, resonant inelastic X-ray scattering (RIXS) or resonant X-ray emission spectroscopy (RXES) offers extended electronic structural information through photon-in photon-out 2-dimensional scans (Fig. 13.2c). In RIXS, the emitted photon energy is scanned as a function of the incident photon energy across the absorption edges[62]. The approach is beneficial in several ways as: (1) it provides the ability to probe occupied (XES) and unoccupied orbitals (XAS) together, and (2) RIXS spectra are better energy-resolved than conventional XAS, where the core-hole lifetime broadens the features of the spectrum. This effect is more significant in the K-edge (1s core hole) than in the L-edge (2p core hole) [39, 62]. So far, RIXS has not been applied as frequently as XAS and XES at XFELs due to the experimental difficulties related with scanning both the X-ray energy of the incoming beam and the emission energy with high-energy resolution. This requires a stable sample delivery for an accurate normalization of signals over the RIXS plane and very good normalization of the scanned incident beam. Below, the possibility of measuring 3d metal RIXS in the hard (1s2p RIXS) and soft X-ray (2p3d RIXS) energy range at XFELs is discussed.

In 1s2p RIXS, hard X-rays, scanned across the K pre-edge, are used to excite a 1s electron into an unoccupied valence orbital (1s to 3d transition). The emission due to the decay of a 3p or 2p electron into the 1s shell is measured as a function of the excitation energy by means of an emission spectrometer (see Fig. 13.1). The energy difference between excitation and emission corresponds to the energy

difference between 2p or 3p and 3d orbitals and, therefore, one can get L-edge-like XAS spectra with the advantages of using hard X-rays (high-excitation energy and therefore high X-ray penetration depth and larger attenuation length) to probe these transitions indirectly. In addition, the RIXS 2D plot makes the background separation of the pre-edge structure from the main K-edge feature easier. At SR facilities, 1s2p RIXS has been used to study several biological systems and proven to be a powerful tool for extracting charge and spin state information of metal centers [63, 64]. In order to enable RIXS measurements at XFELs, however, one needs to overcome several challenges, many of which are common with XAS data collection described above, such as accurate incident beam diagnostics and normalization protocols, both for the incident X-ray intensity and for the sample variations (probing volume and concentration). With the on-going development of sample delivery methods, improved efficiency of the spectrometers, better beamline diagnostics, and the availability of high-repetition rate XFELs, hard X-ray RIXS measurements of dilute biological samples will be more easily accessible in the near future.

Another way of collecting hard X-ray RIXS spectra is by using a transmissive spectrometer to record the XFEL SASE beam spectra (input spectra) shot-by-shot in combination with a dispersive XES spectrometer to collect the emission spectra (output spectra). The XFEL pink beam is composed of multiple peaks exhibiting profound fluctuations from shot to shot in both amplitude and energy. With proper data treatment, these random shot-to-shot spectral fluctuations can be exploited to extract the incidence energy dependence of a signal. The input and output spectra are measured for each shot, and the RIXS map can be reconstructed from input–output correlations. This so-called stochastic spectroscopy approach has been used in other non-X-ray spectroscopic methods [65]. Moreover, a XANES spectrum can be extracted as the integral of the RIXS spectrum over the detected (output) energy axis. This technique eliminates the need for an upstream monochromator, and the corresponding flux loss (up to 99%), which is particularly problematic for dilute samples and photon-hungry experiments like RIXS, in which the photon count rates are very low.

In the soft X-ray regime, pursuing 2p3d RIXS (see electronic transitions in Fig. 13.1) shares common issues with its hard X-ray counterpart (described above), including accurate incident beam diagnostics and normalization protocols. While hard X-ray RIXS is feasible with the current technology, soft X-ray RIXS of dilute biological systems is not presently within reach. The RIXS data collection requires a high-energy resolution (resolving power better than 1000 (i.e., better than 0.6 eV)) on the emitted photons, which can be achieved by a grating spectrometer or by the projected resolution of the so-called TES detector (transition-edge sensor) [66]. The grating spectrometer, however, has yet to become efficient for collecting signals from dilute samples, as it typically covers only 10^{-5} sr of the solid angle and its quantum efficiency is around 10%. While the method has been applied to more concentrated molecular systems [67–69], further development of the spectrometer and optimizing detection efficiency [70, 71] is necessary for the data collection of

dilute systems. In addition, a higher repetition rate of the XFEL pulses such as planned for LCLS-II and European XFEL is required to realize such photon-hungry experiments.

13.4 Applications

For the past few decades, SR-based X-ray spectroscopy has provided valuable insights into the structure and mechanism of metalloenzymes. Many of the SR measurements are carried out at cryogenic temperatures to minimize X-ray radiation damage to the sample. Only with the advent of XFELs has it become possible to collect damage-free X-ray data at room temperature. XFELs have also opened up the possibility of capturing reaction intermediates and chemical dynamics through the catalytic cycle by incorporating in situ reaction-triggering approaches. Yet, many of the methods are still under development and the potential power of X-ray spectroscopy at XFELs has not been fully utilized. We expect to see more studies as the technology advances and more XFEL beamlines become available. Below, we summarize some examples, reported up to now, with a focus on metalloenzymes.

13.4.1 Metalloenzymes

In nature, the water oxidation reaction is accomplished effectively by the oxygen-evolving complex (OEC) in Photosystem II (PSII), a multi-subunit membrane protein in green plants, algae, and cyanobacteria (Fig. 13.4a). This protein uses sunlight to oxidize water, generating most of the oxygen in the atmosphere, while producing reduced compounds that are a major source of our biological and fossil fuel energy:

$$2H_2O \longrightarrow O_2 + 4e^- + 4H^+$$

The OEC in PSII that catalyzes this reaction contains a heteronuclear Mn_4Ca cluster that couples the four-electron oxidation of water with the one-electron photochemistry occurring at the PSII reaction center by acting as the locus of charge accumulation. The OEC cycles through a series of five intermediate S-states (S_0 to S_4), representing the number of oxidizing equivalents stored on the OEC, and releases O_2 before the formation of the S_0-state (Fig. 13.4b). The recent advancement in the PSII crystal structure determination is significant [72] but the geometric information of the Mn_4CaO_5 cluster has to be complemented by electronic structural information to address several key questions of the mechanism of photosynthetic water oxidation. One of these questions is whether Mn-centered or ligand-centered oxidation occurs, which triggers the O–O bond formation at the last step of catalysis. Previous SR-based studies suggested that the electrons are highly

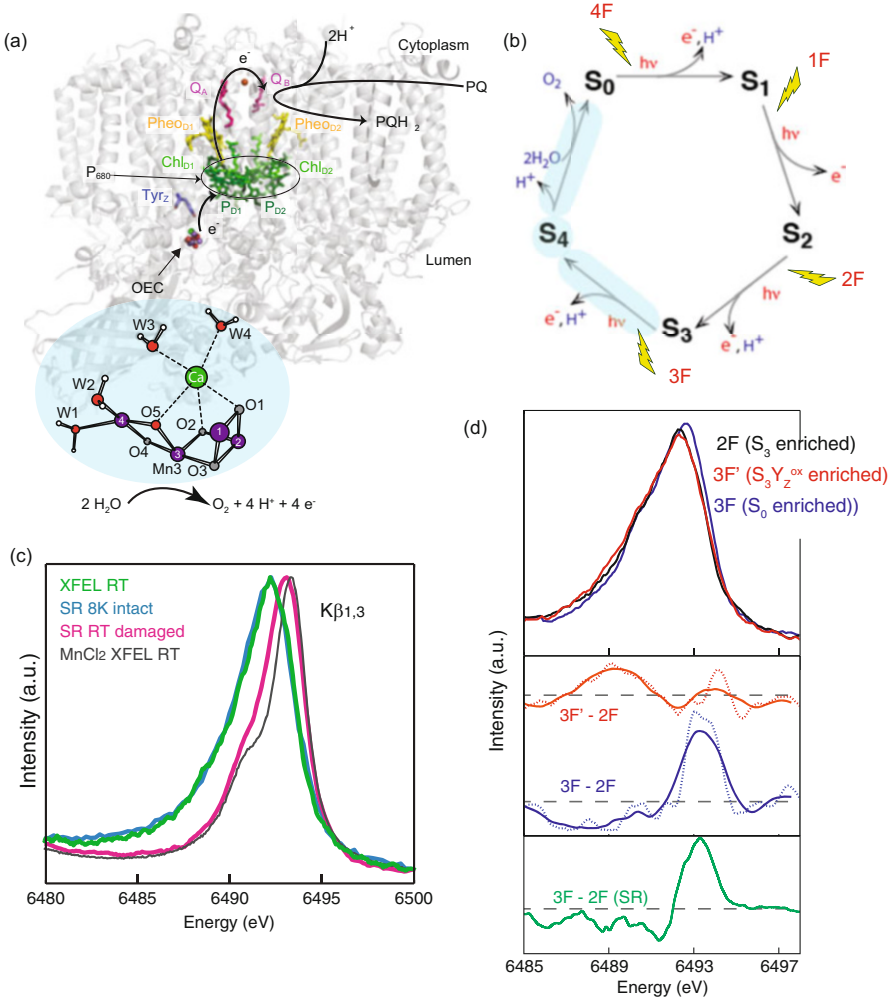

Fig. 13.4 XFEL studies on Photosystem II. **(a)** Structure of PSII and the catalytic site of water oxidation, showing the flow of electrons through the enzyme complex. **(b)** Kok-cycle of photosynthetic oxygen evolution, with states S_0–S_3 being stable intermediates and S_4 a transient state. **(c)** Mn XES of PSII measured at LCLS at room temperature and at SR source at cryogenic temperature, both spectra overlap showing that the LCLS spectra are from the intact sample. Reproduced with permission from [48] **(d)** Mn XES spectra from PSII at room temperature for different flash states, indicating turnover of the samples into the S_3 and the S_0 state and possible indication of a slight oxidation 250 μs into the S_3–S_0 transition. Reproduced with permission from [49]

delocalized in the Mn_4CaO_5 cluster, and that the ligands are intimately involved in charge delocalization, by modulating the covalency of the Mn–O bonds. Therefore, understanding the electronic structure beyond the framework of formal oxidation states under physiological conditions is critical.

Mn $K\beta$ XES from PSII has been collected at multiple hard X-ray instruments of LCLS from solution and crystalline samples [48, 49] (Fig. 13.4c). In these studies, the valence state of the Mn in the OEC was followed through the reaction cycle including time points in the critical S_3 to S_0 step (Fig. 13.4d). As the XES measurement can be performed simultaneously with downstream XRD collection, this method provides a diagnostic capability for X-ray crystallography, since it can also be used as a control to estimate the degree of S-state advancement by the number of laser flashes. The results demonstrate the intactness of the protein during data collection, and the feasibility of measuring X-ray crystallography and spectroscopy to characterize metalloenzymes using the high fluence provided by the XFELs. In parallel to the XES data collection with hard X-rays, there is also an effort to collect Mn L-edge XAS of PSII. In this case, the main challenge is to discriminate the Mn $L\alpha$, β ($2p \rightarrow 3d$) fluorescence at ~640 eV from 4 Mn atoms from the overwhelming O $K\alpha$-edge fluorescence at ~525 eV from ~25,000 O-atoms. Mitzner et al. [36] have introduced a spectrometer based on high transmission reflection zone plates (RZPs) for XAS with PFY detection providing a bandwidth of 20 eV (FWHM), which is enough to discriminate the unwanted signal (see Fig. 13.3a). RZPs have the potential for high-photon detection efficiency with a large solid angle. This setup has been used at LCLS, where a solution sample was delivered with a liquid jet into a vacuum chamber, preventing dehydration of samples and providing a constant sample volume delivery necessary for the XAS data normalization (see Fig. 13.3b). Kubin et al. have shown that it is possible to collect data using a metal concentration of mM-range samples with this approach [37] (see Fig. 13.3c), demonstrating that PFY-XAS with RZPs is a robust approach for collecting dilute metal signals at XFELs.

Cytochrome C, a heme-containing enzyme from the cytochrome family, serves as an electron transfer protein in biological processes as well as a peroxidase enzyme in cellular apoptosis. A single chemical bond, Fe-S(Met), regulates the function of the protein, from transferring electrons to produce energy for cellular respiration when the bond is intact, to triggering the breakdown of the mitochondria when it is broken. The strength of this bond was studied at the XPP [73] endstation of LCLS by photoexciting ferrous cytochrome C with a 520-nm laser, which results in thermal ultrafast photodissociation and recombination of the S(Met) [50]. The protein was delivered to the beam in solution form by a liquid jet and the Fe K-edge XAS and Fe $K\beta_{1,3}$ XES signals were collected using a diode and a von Hamos spectrometer with a 2D detector, respectively (see Fig. 13.5a). The study followed the bond rupture and formation of a five-coordinated high-spin active site with Met recombination at 6.3 ps. This study quantified the protein contribution to keeping the Fe–S(Met) bond under physiological conditions to be 4 kcal/mol, which is derived from an adjacent hydrogen bond network. This contribution is weak enough to allow bond rupture in the presence of cardiolipin, a lipid in the mitochondria's membrane, opening a catalytic ligand-binding site that triggers the programmed cellular death.

In another recent XFEL-based experiment, vitamin B_{12}, or cobalamins, were studied. The vitamin B_{12} family is vital to ensure the proper function of many processes including the production of energy, red blood cells, and the operation

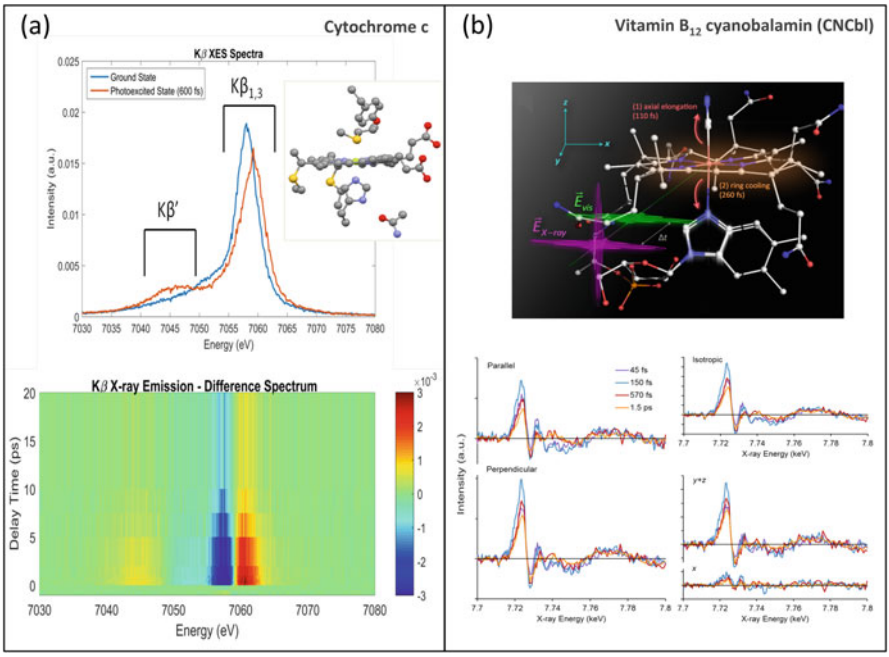

Fig. 13.5 **(a)** Fe $K\beta$ XES spectra cytochrome c, ground (blue) and excited state (red), collected at the LCLS following 520 nm excitation **(top)** and difference spectra showing time dependence up to 20 ps **(bottom)**. Reproduced with permission from [50]. **(b)** Diagram of structural and electronic changes in vitamin B_{12}, cyanocobalamin (CNCbl) following photoexcitation by 550 nm laser wavelength **(top)**. Co K-edge XANES spectra collected at the LCLS. Parallel and perpendicularly polarized time-dependent difference spectra in four representative time regions **(bottom, left)**. Isotropic, x and $y + z$ directions difference spectra derived from the polarization data **(bottom, right)**. Reproduced with permission from [28]

of the nervous system through methyl transfer and radical rearrangement. They also function as gene regulators triggered via photolysis of the Co–C bond. The dynamics of this photochemical reaction mechanism were studied by time-resolved polarized Co XANES and UV/vis spectroscopy by Miller et al. [28] (see Fig. 13.5b). They measured the vitamin B_{12} cofactor cyanocobalamin (CNCbl) in solution photoexcited by a 550-nm fs laser. They were able to separate the directional-dependent components of the reaction dynamics by varying the laser/X-ray polarization angle (Fig. 13.5b). The Co–CN and Co–NIM bonds were shown to elongate in the axial direction of the corrin ring, on a 110-fs timescale. Subsequently, the corrin ring relaxation of the equatorial ligand happens at 260 fs followed by ground state internal conversion on a 6.2-ps timescale. This reaction mechanism describes reactivity, stability, and deactivation of electronically excited cobalamins, which, if understood in detail, will facilitate the development of new targeted medications controlled through light.

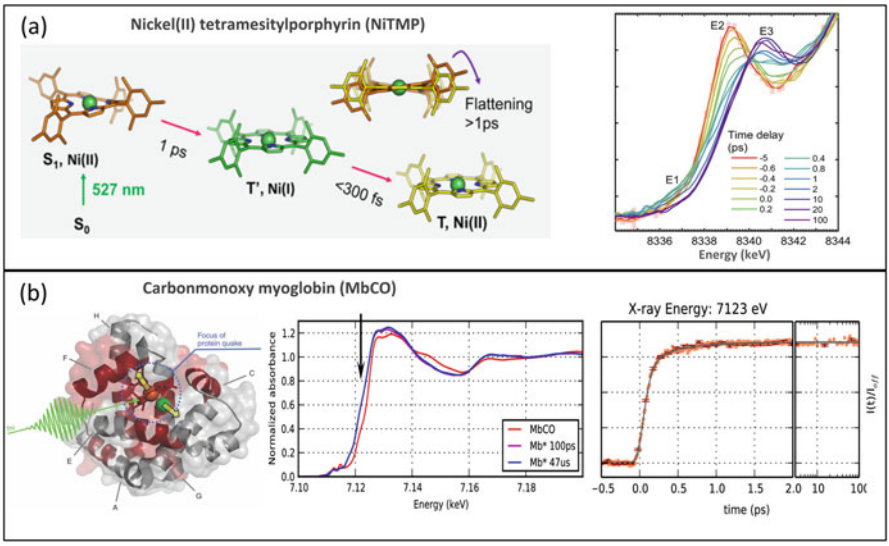

Fig. 13.6 **(a)** Diagram of structural and electronic changes in Nickel(II) tetramesitylporphyrin (NiTMP) following photoexcitation by 527 nm laser wavelength **(left)**. Ni K-edge XANES spectra of NiTMP collected at the LCLS showing the time evolution between 5 and 100 ps after excitation **(right)**. Reproduced with permission from [26] **(b)** Carbonmonoxy myoglobin (MbCO) structure **(left)**. Time-resolved Fe XANES measurements showing the overall spectrum **(center)** and the time trace for absorption changes at 7123 eV **(right)**. Reproduced with permission from [25]

13.4.2 Inorganic Systems Relevant to Biological Systems

Another example of biological relevance was the study of the excited state dynamics of Ni(II) tetramesitylporphyrin (NiTMP) by Shelby et al. [26]. Ni metalloporphyrins undergo a cascade relaxation through multiple electronic states following photoexcitation (see Fig. 13.6a). Some of the states involving metal centers could be regulated catalytically to control the excited state relaxation. It is uncertain if a transient Ni(I) charge transfer state is present in the few ps time domain. Transient Ni K-edge XANES spectra were collected after fs photoexcitation (527 nm) of an NiTMP solution (Fig. 13.6a). Additionally to the spectra of the initial S0 state and the final T(d,d) state (formed within 20 ps), the study shows an intermediate state forming in the sub-ps timescale, which was ascribed by DFT calculations to an Ni(I)(pi,d) electronic state (T'). These results enable the determination of the excited state structural dynamics of NiTMP before thermal relaxation and to resolve intermediates of potential photocatalytic relevance.

The dissociation of the Fe–CO bond in carbonmonoxy myoglobin (MbCO), an Fe- and O-binding protein responsible for the transport of oxygen in muscle tissue, was studied by Levantino and coworkers [25] (see Fig. 13.6b). They collected the

XAS signal in TFY mode after 538 nm laser excitation from a 5.6-mM solution of MbCO transported to the beam through a liquid jet. They monitored changes in the Fe K-edge during the ultrafast (sub ps) photolysis process. By measuring the Fe XANES spectrum at three different energy points using 30 fs short X-ray pulses, they were able to fit the dynamics of this process by two components with characteristic times of 70 fs and 400 fs (Fig. 13.6b). The former was interpreted as the first step of the protein quake (a propagation of the strain released at the active site during the movement of the protein away from the active site), consisting of an Fe out-of-plane motion coupled to the motion of the helix F. The 400 fs process was explained as a residual elongation of the Fe–N bond length in the heme, connected to a contraction of the Fe–His bond. This work serves as a model for studying structural and electronic dynamic processes occurring after photoexcitation of proteins in general.

13.5 Conclusions

In this chapter, we have summarized the current status of X-ray spectroscopic methods and their application to biological systems at XFELs. These new X-ray sources have made X-ray data collection of biological samples under physiological conditions possible, both in the soft and hard X-ray energy regimes, as well as enabling the time-resolved study of fs/ps processes. As mentioned throughout the chapter, further method developments to take full advantage of the XFELs novel characteristics are needed and underway. We expect that high-repetition rate XFELs currently planned will make a big impact in X-ray spectroscopy-based studies, in particular for photon-hungry experiments. We also expect nonlinear X-ray spectroscopy and/or multidimensional X-ray spectroscopy to be realized in the near future, likely expanding the possibility of collecting X-ray spectroscopy data on biological samples. X-ray spectroscopy methods, in combination with structural studies, have the potential to lead to the understanding on how nature controls complicated multi-electron reactions in metalloenzymes by using metal clusters embedded in protein environments.

Acknowledgements R. A.-M. and J.Y. acknowledge all the collaborators of the research presented in this chapter. Use of the Linac Coherent Light Source (LCLS), SLAC National Accelerator Laboratory, is supported by the US Department of Energy, Office of Science, Office of Basic Energy Sciences under Contract No. DE-AC02-76SF00515. J.Y. thanks the Director, Office of Science, Office of Basic Energy Sciences, Division of Chemical Sciences, Geosciences, and Biosciences of the Department of Energy under contract DE-AC02-05CH11231, and the NIH Grants GM110501 and GM055302, which contribute to supporting some of the research presented in this chapter.

References

1. Yano, J., Kern, J., Irrgang, K. D., Latimer, M. J., Bergmann, U., Glatzel, P., et al. (2005). *Proceedings of the National Academy of Sciences of the United States of America, 102*(34), 12047–12052.
2. Garman, E., & Weik, M. (2017). *Journal of Synchrotron Radiation, 24*(1), 1–6.
3. Holton, J. (2009). *Journal of Synchrotron Radiation, 16*(2), 133–142.
4. Lemke, H., Weaver, M., Chollet, M., Robinson, J., Glownia, J. M., Bionta, M. R., et al. (2013). *Proceedings of SPIE, 8778*, 87780S.
5. Margaritondo, G., & Ribic, P. R. (2011). *Journal of Synchrotron Radiation, 18*, 101–108.
6. Emma, P., Akre, R., Arthur, J., Bionta, R., Bostedt, C., Bozek, J., et al. (2010). *Nature Photonics, 4*, 641–647.
7. Ishikawa, T., Aoyagi, H., Asaka, T., Asano, Y., Azumi, N., Bizen, T., et al. (2012). *Nature Photonics, 6*, 540–544.
8. Chapman, H. N., Fromme, P., Barty, A., White, T., Kirian, R., Aquila, A., et al. (2011). *Nature, 470*(7332), 73–77.
9. Nass, K., Foucar, L., Barends, T. R. M., Hartmann, E., Botha, S., Shoeman, R. L., et al. (2015). *Journal of Synchrotron Radiation, 22*(2), 225–238.
10. Boutet, S., Lomb, L., Williams, G. J., Barends, T. R. M., Aquila, A., Doak, R. B., et al. (2012). *Science, 337*, 362–364.
11. Alonso-Mori, R., Kern, J., Gildea, R. J., Sokaras, D., Weng, T.-C., Lassalle-Kaiser, B., et al. (2012). *Proceedings of the National Academy of Sciences of the United States of America, 109*(47), 19103–19107.
12. Weierstall, U. (2014). *Philosophical Transactions of the Royal Society B, 369*, 20130337.
13. Weierstall, U., Doak, R. B., Spence, J. C. H., Starodub, D., Shapiro, D., Kennedy, P., et al. (2008). *Experiments in Fluids, 44*, 675.
14. Roessler, C. G., Kuczewski, A., Stearns, R., Ellson, R., Olechno, J., Orville, A. M., et al. (2013). *Journal of Synchrotron Radiation, 20*, 805–808.
15. Roessler, C. G., Agarwal, R., Allaire, M., Alonso-Mori, R., Andi, B., Bachega, J. F. R., et al. (2016). *Structure, 24*(4), 631–640.
16. Fuller, F. D., Gul, S., Chatterjee, R., Burgie, E. S., Young, I. D., Lebrette, H., et al. (2017). *Nature Methods, 14*(4), 443–449.
17. Milathianaki, D., Boutet, S., Williams, G. J., Higginbotham, A., Ratner, D., Gleason, A. E., et al. (2013). *Science, 342*(6155), 220–223.
18. Wittenberg, J. S., Miller, T. A., Szilagyi, E., Lutker, K., Quirin, F., Lu, W., et al. (2014). *Nano Letters, 14*(4), 1995–1999.
19. Roedig, P., Ginn, H. M., Pakendorf, T., Sutton, G., Harlos, K., Walter, T. S., et al. (2017). *Nature Methods, 14*, 805–810.
20. Koningsberger, D., & Prins, R. (1988). *X-Ray absorption: Principles, applications, techniques of EXAFS, SEXAFS and XANES*. New York: Wiley.
21. Amann, J., Berg, W., Blank, V., Decker, F. J., Ding, Y., Emma, P., et al. (2012). *Nature Photonics, 6*, 693.
22. Kroll, T., Kern, J., Kubin, M., Ratner, D., Gul, S., Fuller, F. D., et al. (2016). *Optics Express, 24*(20), 22469–22480.
23. Lemke, H. T., Bressler, C., Chen, L. X., Fritz, D. M., Gaffney, K. J., Galler, A., et al. (2013). *The Journal of Physical Chemistry A, 117*, 735–740.
24. Cammarata, M., Bertoni, R., Lorenc, M., Cailleau, H., Di Matteo, S., Mauriac, C., et al. (2014). *Physical Review Letters, 113*, 227402.
25. Levantino, M., Lemke, H. T., Schirò, G., Glownia, M., Cupane, A., Cammarata, M., et al. (2015). *Structural Dynamics, 2*(4), 041713.
26. Shelby, M. L., Lestrange, P. J., Jackson, N. E., Haldrup, K., Mara, M. W., Stickrath, A. B., et al. (2016). *Journal of the American Chemical Society, 138*, 8752–8764.

27. Marino, A., Cammarata, M., Matar, S. F., Ltard, J.-F., Chastanet, G., Chollet, M., et al. (2016). *Structural Dynamics, 3*(2), 023605.
28. Miller, N. A., Deb, A., Alonso-Mori, R., Garabato, B. D., Glownia, J. M., Kiefer, L., et al. (2017). *Journal of the American Chemical Society, 139*(5), 1894–1899.
29. Zhu, D., Cammarata, M., Feldkamp, J., Fritz, D., Hastings, J., Lee, S., et al. (2013). *Journal of Physics Conference Series, 425*, 052033.
30. Obara, Y., Katayama, T., Ogi, Y., Suzuki, T., Kurahashi, N., Karashima, S., et al. (2013). *Optics Express, 22*(1), 1105–1113.
31. Katayama, T., Inubushi, Y., Obara, Y., Sato, T., Togashi, T., Tono, K., et al. (2013). *Applied Physics Letters, 103*, 131105.
32. Ogi, Y., Obara, Y., Katayama, T., Suzuki, Y.-I., Liu, S. Y., Bartlett, N. C.-M., et al. (2015). *Structural Dynamics, 2*, 034901.
33. Gaudin, J., Fourment, C., Cho, B. I., Engelhorn, K., Galtier, E., Harmand, M., et al. (2014). *Scientific Reports, 4*, 4724.
34. Stöhr, J. (1992). *NEXAFS spectroscopy*. Berlin: Springer.
35. Friedrich, S., Funk, T., Drury, O., Labov, S., & Cramer, S. (2002). *Review of Scientific Instruments, 73*(3), 1629.
36. Mitzner, R., Rehanek, J., Kern, J., Gul, S., Hattne, J., Taguchi, T., et al. (2013). *Journal of Physical Chemistry Letters, 4*, 3641.
37. Kubin, M., Kern, J., Gul, S., Kroll, T., Chatterjee, R., Löchel, H., et al. (2017). *Structural Dynamics, 4*, 054307.
38. Schreck, S., Beye, M., Sellberg, J. A., McQueen, T., Laksmono, H., Kennedy, B., et al. (2014). *Physical Review Letters, 113*, 153002.
39. Glatzel, P., & Bergmann, U. (2005). *Coordination Chemistry Reviews, 249*(7), 65.
40. Hamos, L. V. (1932). *Naturwiss, 20*, 705–706.
41. Alonso-Mori, R., Kern, J., Sokaras, D., Weng, T.-C., Nordlund, D., Tran, R., et al. (2012). *Review of Scientific Instruments, 83*, 073114.
42. Zhang, W., Alonso-Mori, R., Bergmann, U., Bressler, C., Chollet, M., Galler, A., et al. (2014). *Nature, 509*, 345–348.
43. Zhang, W., Kjr, K. S., Alonso-Mori, R., Bergmann, U., Chollet, M., Fredin, L. A., et al. (2017). *Chemical Science, 8*, 515–523.
44. Canton, S. E., Kjr, K. S., Vank, G., van Driel, T. B., ichi Adachi, S., Bordage, A., et al. (2015). *Nature Communications, 6*, 6359.
45. Haldrup, K., Gawelda, W., Abela, R., Alonso-Mori, R., Bergmann, U., Bordage, A., et al. (2016). *The Journal of Physical Chemistry B, 120*, 1158–1168.
46. Alonso-Mori, R., Asa, K., Bergmann, U., Brewster, A. S., Chatterjee, R., Cooper, J. K., et al. (2016). *Faraday Discussions, 194*, 621–638.
47. Kjr, K. S., Zhang, W., Alonso-Mori, R., Bergmann, U., Chollet, M., Hadt, R. G., et al. (2017). *Structural Dynamics, 4*(4), 044030.
48. Kern, J., Alonso-Mori, R., Tran, R., Hattne, J., Gildea, R. J., Echols, N., et al. (2013). *Science, 340*(6131), 491–495.
49. Kern, J., Tran, R., Alonso-Mori, R., Koroidov, S., Echols, N., Hattne, J., et al. (2014). *Nature Communications, 5*, 4371.
50. Mara, M. W., Hadt, R. G., Reinhard, M. E., Kroll, T., Lim, H., Hartsock, R., et al. (2017). *Science, 356*(6344), 1276–1280.
51. Stojanoff, V., Hamalainen, K., Siddons, D. P., Hastings, J. B., Berman, I. E., Cramer, S., et al. (1992). *Review of Scientific Instruments, 63*(1), 1125–1127.
52. Alonso-Mori, R., Sokaras, D., Zhu, D., Kroll, T., Chollet, M., Feng, Y., et al. (2015). *Journal of Synchrotron Radiation, 22*(3), 612–620.
53. Mori, R. A., Paris, E., Giuli, G., Eeckhout, S. G., Kavcic, M., Zitnik, M., et al. (2009). *Analytical Chemistry, 81*(15), 6516–6525.
54. Mori, R. A., Paris, E., Giuli, G., Eeckhout, S. G., Kavc, M., Zitnik, M., et al. (2010). *Inorganic Chemistry, 49*(14), 6468–6473.

55. Thomas, R., Kas, J., Glatzel, P., Samarai, M. A., de Groot, F. M., Mori, R. A., et al. (2015). *Journal of Physical Chemistry C, 119*(5), 2419–2426.
56. Beye, M., Anniyev, T., Coffee, R., DellAngela, M., Föhlisch, A., Gladh, J., et al. (2013). *Physical Review Letters, 110*, 186101.
57. Nilsson, A., LaRue, J., Öberg, H., Ogasawara, H., Dell'Angela, M., Beye, M., et al. (2017). *Chemical Physics Letters, 675*, 145–173.
58. Dell'Angela, M., Anniyev, T., Beye, M., Coffee, R., Föhlisch, A. Gladh, J., et al. (2013). *Science, 339*(6125), 1302–1305.
59. Shavorskiy, A., Cordones, A., Vura-Weis, J., Siefermann, K., Slaughter, D., Sturm, F., et al. (2013). *AIP Conference Proceedings, 1525*, 475.
60. Kroll, T., Weninger, C., Alonso-Mori, R., Sokaras, D., Zhu, D., Mercadier, L., et al. (2017). *Physical review letters, 120*(13), 133203.
61. Rohringer, N., Ryan, D., London, R. A., Purvis, M., Albert, F., Dunn, J., et al. (2012). English. *Nature, 481*(7382), 488–491.
62. Kotani, A., & Shin, S. (2001). *Reviews of Modern Physics, 73*, 203.
63. Kroll, T., Hadt, R. G., Wilson, S. A., Lundberg, M., Yan, J. J., Weng, T.-C., et al. (2014). *Journal of the American Chemical Society, 136*(52), 18087–18099.
64. Glatzel, P., Schroeder, H., Pushkar, Y., BoronIII, T., Mukherjee, S. G., Christo, V. L., et al. (2013). *Inorganic Chemistry, 52*(10), 5642–5644.
65. Franz, M. O., & Schölkopf, B. (2006). *Neural Computation, 18*(12), 3097–3118.
66. Titus, C. J., Baker, M. L., Lee, S. J., mei Cho, H., Doriese, W. B., Fowler, J. W., et al. (2017). arXiv 1706.09878.
67. Wernet, P., Kunnus, K., Josefsson, I., Rajkovic, I., Quevedo, W., Beye, M., et al. (2015). *Nature, 520*, 78–81.
68. Kunnus, K., Josefsson, I., Rajkovic, I., Schreck, S., Quevedo, W., Beye, M., et al. (2016). *Structural Dynamics, 3*(4), 043204.
69. Eckert, S., Norell, J., Miedema, P.S., Beye, M., Fondell, M., Quevedo, W., et al. (2017). *Angewandte Chemie, International Edition, 56*, 6088.
70. Zhong, Y., Rehanek, J., Löchel, H., Braig, C., Buck, J., Firsov, A., et al. (2017). *Optics Express, 25*(10), 10984–10996.
71. Qiao, R., Li, Q., Zhuo, Z., Sallis, S., Fuchs, O., Blum, M., et al. (2017). *Review of Scientific Instruments, 88*(3), 033106.
72. Umena Y., Kawakami, K., Shen, J.-R., & Kamiya, N. (2011). *Nature, 473*, 55–60.
73. Chollet, M., Alonso-Mori, R., Cammarata, M., Damiani, D., Defever, J., Delor, J. T., et al. (2015). *Journal of Synchrotron Radiation, 22*(3), 503–507.